ACS APPLIED MATERIALS & INTERFACES

www.acsami.org

Research Article

Charge Dynamics of a CuO Thin Film on Picosecond to Microsecond Timescales Revealed by Transient Absorption Spectroscopy

Mona Asadinamin, Aleksandar Živkovic, Susanne Ullrich,* Henning Meyer,* and Yiping Zhao*

Cite This: *ACS Appl. Mater. Interfaces* 2023, 15, 18414−18426

Read Online

ACCESS | Metrics & More | Article Recommendations | Supporting Information

ABSTRACT: Understanding the mechanism of charge dynamics in photocatalysts is the key to design and optimize more efficient materials for renewable energy applications. In this study, the charge dynamics of a CuO thin film are unraveled via transient absorption spectroscopy (TAS) on the picosecond to microsecond timescale for three different excitation energies, i.e., above, near, and below the band gap, to explore the role of incoherent broadband light sources. The shape of the ps-TAS spectra changes with the delay time, while that of the ns-TAS spectra is invariant for all the excitation energies. Regardless of the excitations, three time constants, $\tau_1 \sim 0.34-0.59$ ps, $\tau_2 \sim 162-175$ ns, and $\tau_3 \sim 2.5-3.3$ μs, are resolved, indicating the dominating charge dynamics at very different timescales. Based on these observations, the UV−vis absorption spectrum, and previous findings in the literature, a compelling transition energy diagram is proposed. Two conduction bands and two defect (deep and shallow) states dominate the initial photo-induced electron transitions, and a sub-valence band energy state is involved in the subsequent transient absorption. By solving the rate equations for the pump-induced population dynamics and implementing the assumed Lorentzian absorption spectral shape between two energy states, the TAS spectra are modeled which capture the main spectral and time-dependent features for $t > 1$ ps. By further considering the contributions from free-electron absorption during very early delay times, the modeled spectra reproduce the experimental spectra very well over the entire time range and under different excitation conditions.

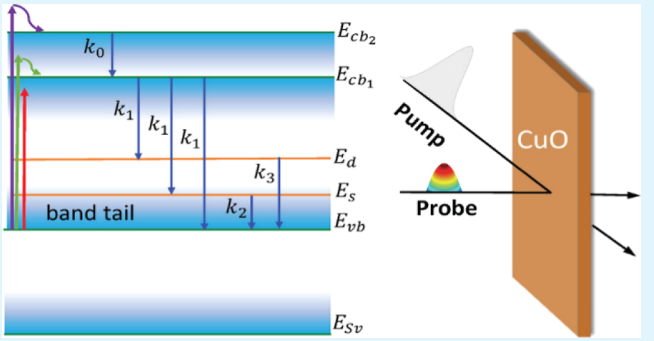

KEYWORDS: *CuO, transient absorption spectroscopy (TAS), model, energy diagram, rate equations, photocatalysts*

1. INTRODUCTION

Photocatalysts have various important energy and environmental applications, such as solar-water splitting, solar CO_2 conversion, and antimicrobial/antiviral activity.[1,2] All these applications involve at least two processes: photocarrier generation in which light excites the photocatalyst to generate radicals such as reactive oxygen species (ROS) and photocatalysis reactions in which ROS react with the desired chemical species surrounding the photocatalyst.[3,4] In the first process, the dynamics of the photoexcited charge carriers in photocatalysts is the limiting factor which determines the concentration of the ROS products, while in the second process the reaction kinetics and dynamics play the most important role. Intrinsically, the charge dynamics occur on different timescales; i.e., the relaxation of hot charge carriers occurs in less than 1 picosecond (ps), recombination and de-trapping occur in a nanosecond (ns) to microsecond (μs) or even millisecond (ms) timescale, while photocatalysis reactions, i.e., reduction, oxidation, or redox reactions, occur in μs to s timescale.[5−7] Clearly, there is a mismatch between the timescale of the intrinsic dynamics of photocarriers and chemical reactions, which demands a thorough investigation of their relationship across a broad timescale. Therefore, understanding the dynamics of photoexcited charge carriers over an extended time range is critical. One of the most frequently used tools to investigate photocarrier dynamics is transient absorption spectroscopy (TAS), which provides essential information about both the time-dependent and spectral characteristics of the charge dynamics.

So far, most TAS studies are mainly focused on either the ultra-fast (fs to ps) or long (ns to s) timescales which can only provide an incomplete picture of the charge dynamics.[8,9] In addition, many of them are only concentrated on the time-dependent behavior at specific probe photon energies (i.e., selected wavelengths in the TAS spectrum) and neglect the overall spectral changes as a function of time.[7,10] In principle, the time-dependent behavior of the spectra in different

Received: December 15, 2022
Accepted: March 21, 2023
Published: March 30, 2023

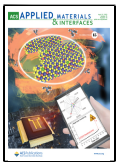

wavelength regions should be different because they may correspond to different transitions and reveal important information on the energy states involved within the photocatalysts. However, only a handful of papers reported a simultaneous analysis of spectral and time-dependent behavior. For example, Cooper et al. emphasized the importance of simultaneous disentangling of spectral and kinetics behavior in TAS spectra and proposed a comprehensive energy diagram for $BiVO_4$ by combining optical properties of the material with the known mechanisms of band edge broadening, band-gap alterations, and free-carrier absorption.[11] Yoshihara et al. analyzed the spectral behavior of TiO_2 films to extract the contributions of electrons and holes in the charge dynamics.[12] Kollenz et al. introduced a deep-learning-based approach to elucidate the charge dynamics of materials by simultaneous analysis of spectral and kinetic dependence of TAS spectra of lycopene in tetrahydrofuran.[13] Furthermore, in many photocatalytic-based applications, an incoherent broadband light source is used, enabling the photocatalyst to utilize different electronic transitions triggered by different energies. Thus, to better understand the roles of different energy states in photocatalysis processes under a broadband illumination, it is beneficial to investigate the photocarrier charge dynamics at different excitation energies. Therefore, in order to obtain a complete picture of the charge dynamics of a photocatalyst, one should conduct a broad timescale investigation, from ps to μs (or even ms); perform simultaneous analysis of the spectral and time-dependent behaviors under different excitation energies; and explain the observed results comprehensively.

Here, we attempt to implement the above-mentioned strategy to investigate the charge dynamics of a CuO thin film using ps- and ns-TAS. CuO is an earth-abundant, photostable, sustainable p-type metal oxide[14−17] and has an optical band gap (E_g) of 1.5−2.2 eV.[18−21] It has been widely used for photocatalytic applications[22−25] and photoelectrochemical cells[26,27] and has been reported as an excellent candidate for large-scale photovoltaic deployment.[28] However, there have been only a few experimental studies on the charge dynamics of CuO. Othonos et al. studied the charge carrier relaxation in CuO nanowires (E_g = 1.5 eV) via picosecond—transient absorption spectroscopy (ps-TAS) (only up to 8 ps) using an excitation energy $h\nu_p$ (h is the Planck's constant and ν_p is the frequency of the excitation beam) of 3.1 eV.[29] By analyzing the time-dependent behavior at different probe energies, they reported two time constants, 0.4, and 2.1 ps, which were associated with the hole relaxation from the sub-valence band (SVB) states to the hole states above the valence band (VB).[29] Born et al. studied the ultra-fast charge dynamics of CuO nanocrystals (E_g = 1.55 eV) (only up to 20 ps) with $h\nu_p$ = 1.6 eV, i.e., exciting electrons near the conduction band (CB) edge. The authors only probed the charge dynamics at 0.8 eV, corresponding to a mid-gap energy, which was claimed to be sensitive to the carrier dynamics of the holes near the VB. Based on their time-dependent analysis, three time constants were reported: 330−640 fs corresponding to the momentum relaxation via carrier−carrier scattering in the VB, 2 ps for the energy relaxation via carrier-phonon scattering within the VB, and 50 ps due to the trapping and recombination. Shenje et al. investigated the photocarrier dynamics of a CuO thin film (E_g = 2.2 eV) up to 150 ps with $h\nu_p$ = 3.1 eV.[19] Three time constants were obtained, 250 fs, 2.5 ps, and >150 ps, which were attributed to the previously suggested mechanisms by Born et al.[18] The authors also proposed a possible energy diagram and electronic transitions for the CuO thin film by considering the Urbach tail which represented defect states at 0.2 eV above the VB. Although these previous studies have revealed some essential features of the charge dynamics of CuO, there is a discrepancy in the reported time constants, which could be due to the variations in materials, the limited timescale of the measurements, and the different excitation energies employed by these groups. Thus far, no comprehensive study has been carried out to understand the overall time-dependent spectral behavior in CuO TAS nor extended to a broad timescale, i.e., ps to μs timescale. Moreover, all the previous studies are limited to a single excitation energy. Clearly, a comprehensive understanding and a solid picture of the carrier dynamics of CuO are yet to be determined.

Herein, we carried out systematic experiments to probe the charge dynamics of a CuO thin film from the ps to μs timescale using both ps-TAS and ns-TAS under three different excitation energies: above, near, and below E_g. The overall TAS spectra revealed three time constants, ∼0.5 ps, ∼170 ns, and ∼2.8 μs, which dictated three time evolution regions: ultra-fast, quasi-static, and recovery stages. The TAS spectral features indicated that there exist two intrinsic absorptions near and above E_g, one at ∼2.2 eV (E_g) and the other at ∼2.7 eV. Based on these experimental results and density functional theory calculations in the literature, a comprehensive transition energy diagram with the energy states contributing to the TAS experiments and possible electronic transitions were proposed. Rate equations based on the above assumptions were established, and the time-dependent spectra, which were based on Lorentzian spectral functions for each allowed electron transition, were found to reasonably agree with the experimental findings. These results support our proposed strategy; i.e., to gain a complete picture of the charge dynamics of a photocatalyst, one needs to conduct systematic TAS investigations over an extended time range with varied excitation energies and thoroughly analyze the time-dependent spectra. Such a strategy is also expected to help us establish better insights into the carrier dynamics of a photocatalyst and the corresponding photocatalytic reactions.

2. EXPERIMENTAL SECTION

2.1. Materials. Copper shots (99.9+%) were purchased from Kurt J. Lesker (Clairton, PA). Cleaned glass microscope slides (Gold Seal catalog no. 3010) were used as the substrates for material deposition. Deionized water (18 MΩ cm) was used to prepare all solutions.

2.2. Sample Preparation. A 50 nm Cu thin film was deposited onto the glass substrates by a custom-designed electron-beam deposition system. Glass substrates (3.3 × 1 cm^2) were cleaned by a piranha solution using a 4:1 mixture of sulfuric acid (H_2SO_4) and hydrogen peroxide (H_2O_2) solutions, boiled for about 10 min, rinsed 6 times by deionized water, dried under nitrogen flow, and subsequently mounted into the deposition chamber. The cleaned glass substrates were loaded onto the deposition chamber, and the chamber was pumped down to a base pressure of 3 × 10^{-6}Torr. During the deposition, the pressure was maintained at about ≤6 × 10^{-6} Torr. The deposition rate (0.02 nm s^{-1}) and thickness of the Cu thin film (50 nm) were monitored by a quartz crystal microbalance. The as-deposited Cu thin films were then oxidized in a quartz tube furnace (Lindberg/Blue M Company) at a preset temperature of 380 °C, under an oxygen flow (20 SCCM) for 3 h. During the annealing, the temperature was ramped at a rate of 5 °C min^{-1}. After oxidation, the resulting CuO thin film was determined to be 100 nm thick by atomic force microscopy (Park Systems NX-10 AFM). Three other sets of samples were prepared over a year to confirm reproducibility.

https://doi.org/10.1021/acsami.2c22595
ACS Appl. Mater. Interfaces 2023, 15, 18414−18426

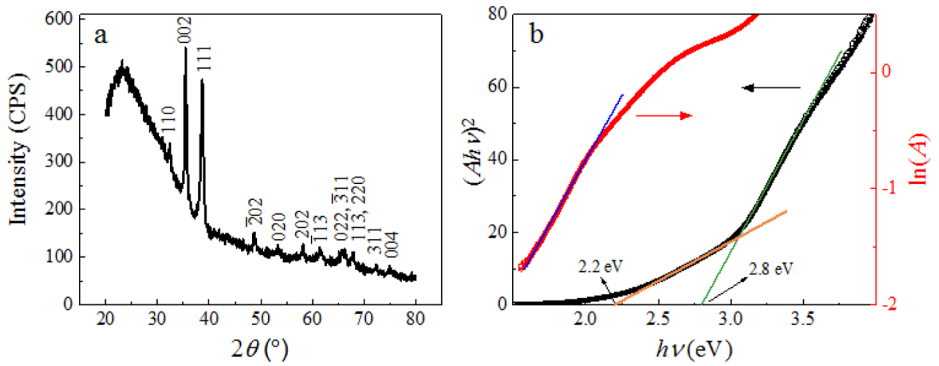

Figure 1. (a) XRD pattern and (b) optical analysis of the CuO thin film. The black curve (left axis) in (b) corresponds to the Tauc plot, and the red curve (right axis) is a semi-log plot of absorption A.

2.3. General Characterization. The crystal structure of the oxidized sample was characterized using a PANalytical X'Pert- PRO MRD X-ray diffractometer (XRD) at a fixed incidence angle of 0.5°. The XRD pattern was recorded with a Cu $K\alpha_1$ radiation (λ = 0.154 nm) in the 2θ range from 20 to 80° in increments of 0.010°. The optical transmission spectra of the sample were measured using a dual-beam UV−visible (UV−vis) spectrophotometer (Shimadzu-UV2450) over the energy range of 1.5−4.1 eV (300−820 nm wavelength range).

2.4. Picosecond-Transient Absorption Spectroscopy. A custom-built setup was used for the ps-TAS measurements. The detail of the setup is explained elsewhere.[30] Briefly, an 800 nm laser pulse with a temporal width of 130 fs was initially generated by a commercially available regenerative amplifier (Coherent Inc Legend Elite seeded by a Mira Optima 900) with a repetition frequency of 1 kHz; the output was used to feed a traveling wave optical parametric amplifier (TOPAS-C) in order to generate the excitation beam at $h\nu_p$ = 3.5 eV (355 nm), 2.2 eV (565 nm), and 1.7 eV (740 nm) with pulse energies of 2, 5.7, and 4.3 μJ, respectively.

At a specific probe beam frequency ν and a time delay t, the absorption difference spectrum, i.e., the TAS spectrum $\Delta A(\nu,t)$, was determined by

$$\Delta A(\nu, t) = A(\nu, t) - A(\nu, \infty) \quad (1)$$

where $A(\nu,t)$ and $A(\nu,\infty)$ are the absorption spectra at a time delay t and in a steady state, respectively. These absorption spectra were determined by taking the negative natural logarithm of the measured transmission spectra with and without the excitation beam. The Surface Xplorer (Ultrafast Systems LLC) software package was used to process the raw data.

2.5. Nanosecond-Transient Absorption Spectroscopy. A transient absorption spectrometer for the ns to μs timescale was set up using the output of a Nd-YAG (Spectra Physics GCR150-10) pumped dye laser (LAS LDL2005) as the excitation source. The system was operated at 10 Hz and provided excitation pulses of about 5 ns duration. In case the output of the dye laser was frequency doubled in a non-linear crystal (KDP or BBO), the fundamental was separated from the second harmonic using a CaF_2 Pellin−Broca prism. In this setup, the accessible excitation wavelengths ranged from 450 to 740 nm and from 225 to 370 nm. A continuous IR filtered output of a Xe arc lamp (Oriel 66001) was used as the probe light. For ns-TAS measurements, the pump beam hit the sample under an angle of 6° from the normal, while the probe light propagated along the normal. The divergent probe beam was collimated before and after the sample with 200 and 300 mm plano-convex lenses, respectively. The probe beam after the sample was analyzed with a monochromator (ARC SpectraPro 150) and detected with a photomultiplier (Electron Tubes: 9813B; housing B2F/RFI). In order to reduce the load on the photomultiplier tube (PMT), a phase-locked chopper (Thorlabs MC 2000B-EC) with a 10% duty cycle blade was used to modulate the probe beam. The time-dependent signal of the PMT was recorded and averaged with a fast digital scope (Tektronix DS684C). The complete system had an overall time response of 15 ns. A computer-controlled shutter allowed to simultaneously block the pump and probe beams, thus realizing a baseline subtraction that efficiently removed the electrical noise due to the firing of the YAG laser. Background signals due to scattered light from the pump laser were suppressed using different combinations of dichroic filters.

3. RESULTS AND DISCUSSION

3.1. Structure and Optical Properties of the CuO Thin Film. Figure 1a shows the XRD pattern of the CuO thin film. All of the observed peaks correspond to the characteristic crystalline planes of CuO (PDF#80-1268), and the thin film does not contain any other phases of copper oxide compounds within the detection limit of the XRD system. Scherrer's equation was used to estimate the crystallite size D,[31]

$$D = \frac{s\lambda}{\beta \cos\theta} \quad (2)$$

where s is the shape factor, λ is the X-ray wavelength, β is the full-width-at-half-maximum of the dominant peaks, and θ is the angle of the dominant peak. λ = 0.154 nm, and for the CuO thin film, the shape factor is assumed to be s = 0.9.[32] The dominant peaks in Figure 1a at (002) and (111) surfaces are at θ = 17.7 and 19.3°, where β = 0.39 and 0.50°, respectively. The estimated crystallite size is D = 16−18 nm, within the range of the reported values for CuO thin films in the literature.[33] The relatively small average crystallite size compared to the thickness of the CuO film (100 nm) indicates the existence of many interfacial boundaries in the thin film, which breaks the periodicity of the crystal and induces more defect, surface, and amorphous states.

The typical optical absorption spectrum of the CuO thin film is shown in Figure S1. It exhibits a non-zero absorption at photons energies $h\nu$ as small as 1.5 eV. The absorption monotonically increases from 1.5 to 3 eV and then increases more rapidly for $h\nu$ > 3 eV. The direct band gap, E_g, of the film is estimated by a Tauc plot shown in Figure 1b (the black curve) according to

$$(Ah\nu)^2 = C(h\nu - E_g) \quad (3)$$

where A is the absorption and C is the proportionality constant. The black curve in Figure 1b is the $(Ah\nu)^2$ *versus* $h\nu$ plot and demonstrates two linear regions: the one fitted by an orange line gives a band gap of E_g = 2.2 ± 0.08 eV, whereas the other region fitted by the green line results in a band-gap-like energy of E_l = 2.8 ± 0.1 eV. The observation of such dual

https://doi.org/10.1021/acsami.2c22595
ACS Appl. Mater. Interfaces 2023, 15, 18414−18426

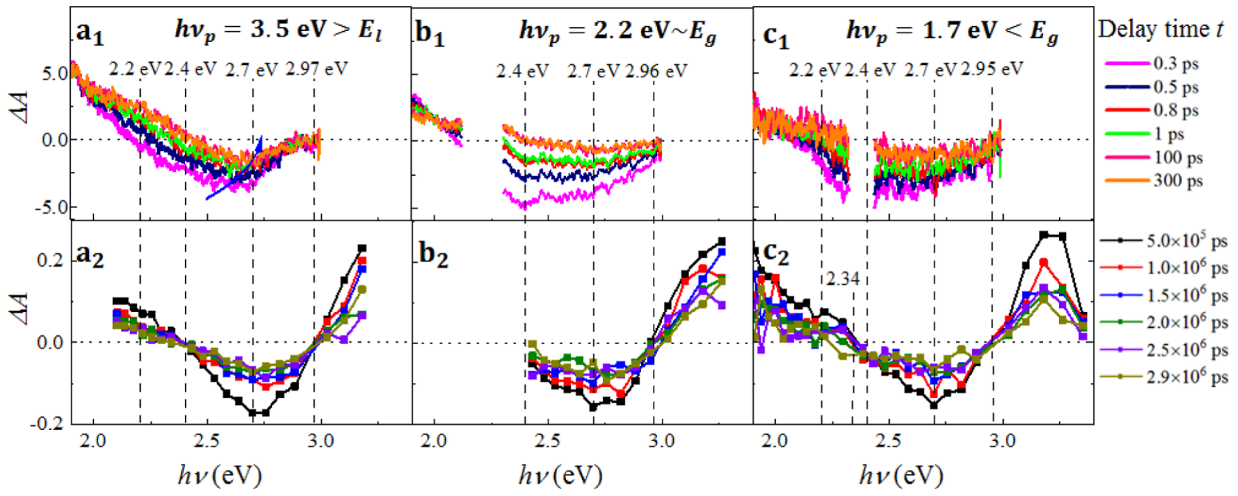

Figure 2. Rescaled ps- and ns-TAS spectra $\Delta A(\nu,t)$at different delay times t under (a) $h\nu_p$ = 3.5 eV > E_l, (b) $h\nu_p$ = 2.2 eV ~ E_g, and (c) $h\nu_p$ = 1.7 eV < E_g. Top row: ps-TAS spectra in the ps timescale; bottom row: ns-TAS spectra in the ns to μs timescale.

band-gap-like behavior will be elaborated in more detail in Section 4.

Since the crystal size of CuO is very small, it is expected that the crystal lattice is significantly distorted, which can introduce a band tail, i.e., an Urbach tail,[34] above the VB and below the CB. The width of the Urbach tail can be estimated by[35]

$$A = A_0 e^{(h\nu - E_0)/E_U} \quad (4)$$

where A_0 and E_0 are related to the material's intrinsic properties, and E_U is the Urbach energy or the tail width. The red curve in Figure 1b is a semi-log plot of A versus $h\nu$; from the slope of the linear fit (the blue line), E_U = 0.5 ± 0.01 eV is extracted, which is within the range of the reported values of 0.2−0.7 eV for CuO in the literature.[33]

3.1.1. Transient Absorption Spectroscopy. As discussed in Section 1, in order to gain a complete picture of charge dynamics, it is suggested that one needs to use different excitation energies to systematically examine the change of TAS. In the meantime, for CuO, there exists a dual band-gap-like behavior as revealed by Figure 1b. Moreover, the UV−vis spectrum in Figure S1 of the Supporting Information shows a non-zero absorption at $h\nu < E_g$ due to the band tail or defect absorption. Therefore, to gain a comprehensive understanding of the charge dynamics of the CuO thin film, it is necessary to investigate the TAS spectra under at least three excitation energies, $h\nu_p > E_l$, $h\nu_p \sim E_g$, and $h\nu_p < E_g$. Both ps- and ns-TAS measurements were conducted for $h\nu_p$ = 3.5, 2.2, and 1.7 eV. To establish a quantitative comparison among TAS spectra in different timescales and $h\nu_p$, all of the obtained TAS spectra $\Delta A(\nu,t)$ were rescaled by the number density of the absorbed photons, $N = \frac{A(h\nu_p)P}{h\nu_p}$, where $A(h\nu_p)$ is the absorption at the excitation energy $h\nu_p$ and P is the power per area of the excitation beam. Figure 2 shows the rescaled $\Delta A(\nu,t)$ spectra as obtained by the ps-TAS (top panel) and ns-TAS (bottom panel) at different $h\nu_p$. It should be noted that the full spectra for the case of $h\nu_p$ = 2.2 eV, as shown in Figure 2b, were not accessible due to the inevitable scattering of the excitation beam.

Figure 2a$_1$ shows the representative rescaled ps-TAS $\Delta A(\nu,t)$ at $h\nu_p$ = 3.5 eV > E_l at different delay times t. Three main spectral features are observed: (1) positive $\Delta A(\nu,t)$ at $h\nu$ < ~2.2 eV; (2) a broad dip centered at ~2.7 eV with an initial width of ~0.8 eV, much broader than the other p-type semiconductors such as ZnO with a width of ~0.2 eV;[36] and (3) a slight blue shift of the dip position as indicated by the blue arrow in the figure. Measurements at the different locations of the sample, as shown in Figure S2, revealed that the broad dip might consist of two dips, one at 2.23 eV and the other at 2.67 eV. Regarding the time dependence of the spectra in Figure 2a$_1$, as t increases, up to ~1 ps, the entire spectra move up, whereas after 1 ps, they remain fairly steady. Figure 2a$_2$ shows the representative ns-TAS $\Delta A(\nu,t)$. The overall spectral shapes are highly comparable to those observed in the ps-TAS $\Delta A(\nu,t)$, with an additional positive $\Delta A(\nu,t)$ present at $h\nu$ > 3 eV. As t increases, the width and position of the broad dip remain unchanged, while both the positive and negative ΔA approach zero. It seems that the spectral shape of the ns-TAS $\Delta A(\nu,t)$ is invariant as a function of t. To confirm the spectral shape changes, the time-dependent $\Delta A(\nu,t)$ in Figure 2a$_1$,a$_2$ are normalized by the absolute value of the dip minima and are shown in Figure S3a1,a2, respectively. The shape of the normalized ns-TAS spectra is time invariant, indicating that the mechanisms for charge dynamics in the ns to μs timescale remain the same, i.e., due to the decay of charge carriers from the trap states. However, the normalized ps-TAS spectra show a strong time dependence: the positive $\Delta A(\nu,t)$ at $h\nu$ < ~2.2 eV becomes more pronounced at $t \leq 1$ ps and is steady afterward. Such a time dependence of the spectral shape indicates that more than one competing mechanism dominates the charge dynamics in the ps timescale. It is noteworthy that the three samples prepared over a year have shown consistent TAS spectra (Figure S4) which confirm the reproducibility.

In the case of $h\nu_p$ = 2.2 eV ~ E_g, the ps-TAS $\Delta A(\nu,t)$ in Figure 2b$_1$ shows the main features observed for the previous case (Figure 2a$_1$). The time dependence trends of the ps-TAS spectra are also similar to the $h\nu_p$ = 3.5 eV case (Figure 2a$_1$). The spectral shape and time dependence of ns-TAS (Figure 2a$_2$) shown in Figure 2b$_2$ are analogous to the case of $h\nu_p$ = 3.5 eV, except for a slightly faster recovery rate in the initial few hundred ns. The normalized spectra in Figure S3b demonstrate the time invariance of the ns-TAS spectral shape and the strong time dependence of the ps-TAS spectra, consistent with the observations in the case of $h\nu_p$ = 3.5 eV.

https://doi.org/10.1021/acsami.2c22595
ACS Appl. Mater. Interfaces 2023, 15, 18414−18426

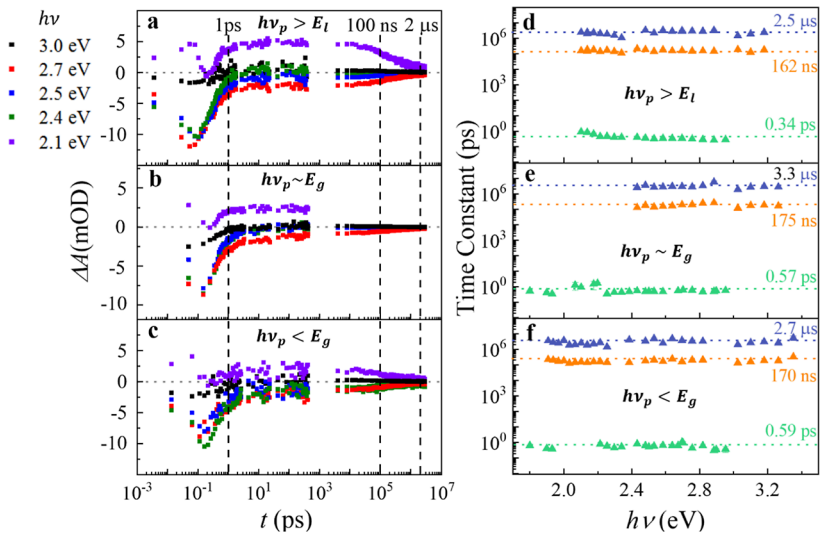

Figure 3. Time traces (ΔA versus t plot at a fixed $h\nu$) at different $h\nu$ under (a) $h\nu_p > E_l$, (b) $h\nu_p \sim E_g$, and (c) $h\nu_p < E_g$ and (d–f) their corresponding resolved time constants.

For the $h\nu_p$ = 1.7 eV < E_g case as shown in Figure 2c, the overall spectral features and time dependence for ps-TAS and ns-TAS $\Delta A(\nu,t)$ are comparable to those of $h\nu_p \sim$ 3.5 eV and $h\nu_p \sim$ 2.2 eV. Regarding the ns-TAS $\Delta A(\nu,t)$, it is worth noting that since the ns-TAS spectra cover a wider range of probe energies, they reveal the existence of a peak centered at ~3.1 eV. The normalized spectra shown in Figure S3c confirm the same observations as in both cases of $h\nu_p$ = 3.5 eV and $h\nu_p$ = 2.2 eV.

To better understand the time dependence of the TAS spectra in both ps and ns timescales, time traces at selected $h\nu$ values ranging from 2.1 to 3.0 eV and for the three different $h\nu_p$ cases from the sub-ps to μs timescale are plotted in Figure 3a–c. The $h\nu$ range covers two distinct spectral regions, the positive $\Delta A(\nu,t)$region at $h\nu \leq$ 2.4 eV and the dip region at 2.4 eV $\leq h\nu \leq$ 3 eV. Note that since the ps and ns measurements are performed via two different setups, combining the data requires a specific strategy; herein, the ns time traces are rescaled such that the starting spectral value of the ns time trace aligns with the end spectral value of the ps time trace (at $t \sim$ 600 ps).

For $h\nu_p > E_l$ as shown in Figure 3a, beyond the ps instrument response region (t > 0.15 ps), the time traces at different $h\nu$ show a similar trend throughout the entire probed timescale: there is an initial rise at $t \leq$ 1 ps, followed by a quasi-static region in 1 ps $\leq t \leq$ ~100 ns, and the subsequent recovery to equilibrium at $t >$ ~100 ns. For the low probe energy region ($h\nu$ = 2.1) eV, $\Delta A(\nu,t)$ is always positive, and the time traces initially rise, moving away from equilibrium, but plateau until a full decay in $t \geq$ 100 ns. The time trace at the low energy isosbestic point ($h\nu \sim$ 2.4 eV) quickly approaches zero from a large negative value in the beginning, then fluctuates around zero. The broad dip, represented by $h\nu$ = 2.5 and 2.7 eV, remains negative throughout the entire timescale; the $\Delta A(\nu,t)$ values increase and approach almost zero within less than 1 ps, reach a quasi-static region, and then gradually decay toward zero. The $\Delta A(\nu,t)$ value at the higher energy isosbestic point ($h\nu$ = 3.0 eV) always fluctuates around zero. In the case of $h\nu_p$ = 2.2 eV ~ E_g, as shown in Figure 3b, the time traces are very similar to those for the $h\nu_p$ = 3.5 eV case, except that $h\nu$ = 3.0 eV, where $\Delta A(\nu,t)$ obviously approaches zero at t < 1 ps. The time traces for the $h\nu_p$ = 1.7 eV < E_g case shown in Figure 3c exhibit much higher noise, but the overall time-dependent trends are very similar to those of the previous two cases.

The time traces are fitted by a linear combination of two or three exponential functions. Some representative fitting results are shown in Figures S5 and S6, respectively. It appears that the use of two exponential functions is insufficient to capture the dynamics in the ns timescale, whereas the use of three exponential functions, i.e., three time constants, results in a reasonable match with the experimental time traces. The extracted time constants τ_1, τ_2, and τ_3 as a function of the probe energy $h\nu$ under different $h\nu_p$ are shown in Figure 3d–f. For all the three $h\nu_p$ cases, the fitted time constants are almost invariant with respect to $h\nu$. For $h\nu_p > E_l$ as shown in Figure 3d, the extracted average time constants are: τ_1 = 0.34 ± 0.13 ps, τ_2 = 162 ± 10 ns, and τ_3 = 2.5 ± 0.3 μs; for the $h\nu_p \sim E_g$ case as shown in Figure 3e, τ_1 = 0.57 ± 0.12 ps, τ_2 = 172 ± 18 ns, and τ_3 = 3.3 ± 0.1 μs, which are slightly higher than the corresponding values in the previous case; for $h\nu_p < E_g$ (Figure 3f), τ_1 = 0.59 ± 0.09 ps, τ_2 = 170 ± 19 ns, and τ_3 = 2.7 ± 0.1 μs. Clearly, regardless of $h\nu_p$, all three time constants are quite consistent with respect to each other, which demonstrates the robustness of the results.

The fastest time constant, 0.3–0.59 ps, agrees with the reported values of 0.25–0.4 ps in the literature,[18,19,29] which have been suggested to arise from the carrier–carrier scattering between two different energy bands. The two slow time constants around 160–175 ns and 2.5–3.3 μs are not reported in any previous literature. Nanosecond time constants are suggested to come from the recombination of charge carriers in shallow defect traps; for example, 5–12 ns was reported for TiO_2[37] and 3.1 ns for WSe_2,[38] while for the deep defect traps, 7 μs in TiO_2[39] and 1–10 μs in a metal halide perovskite[40] were reported. However, another time constant of ~2.5 ps has been suggested in the literature,[18,29] which is not observed in the current study. This missing time constant could be rationalized through different perspectives; for instance, Born et al.[18] used a single probe energy at 0.8 eV which is well below our probe energy range (1.9–3.0 eV) and thus does not allow for a direct comparison. Moreover, the morphology could play a role in

https://doi.org/10.1021/acsami.2c22595
ACS Appl. Mater. Interfaces 2023, 15, 18414–18426

terms of the crystallite sizes. Born et al.[18] used CuO nanocrystals with a diameter of 50 nm and thickness of 20 nm, whereas in our study, the films are 100 nm thick with a crystallite size of 16−18 nm. Othonos et al.,[29] on the other hand, fabricated CuO nanowires with a diameter of ≤200 nm and lengths of up to 10 μm which is much larger than those of our sample. This difference in size could induce different defect states and grain boundaries that impact the recombination time.

4. ENERGY DIAGRAMS AND RATE EQUATION MODELING

In order to understand the complex charge dynamics of the CuO thin film as revealed by Figures 2 and 3, a transition energy diagram with the possible transitions and corresponding rate equations are proposed based on the experimental results and previous literature reports. A simple absorption model is used to find the TAS spectra based on the solutions of the rate equations and estimated initial conditions under different $h\nu_p$. The modeled spectra capture both the spectral and time-dependent behavior of the CuO thin film from the ps to μs timescale.

4.1. Proposed Transition Energy Diagram and Transitions. The proposed energy diagram and the corresponding transitions for the three different excitation cases for the CuO thin film are shown in Figure 4. The model

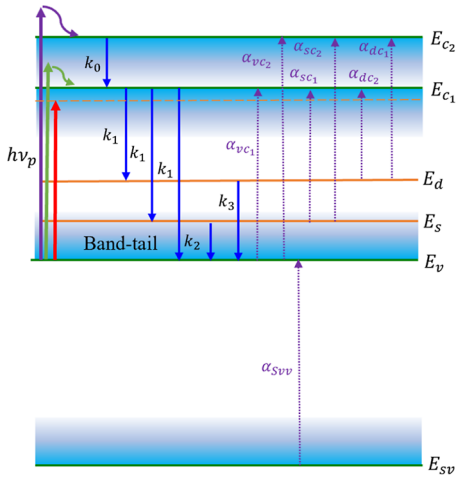

Figure 4. Proposed energy diagram consists of 6 energy states: E_{sv}, E_v, E_s, E_d, E_{c_1}, and E_{c_2}. The blue-gradient areas show the band tails of VB and CB. The purple, green, and red arrows on the left represent three excitation cases: $h\nu_p > E_l$, $h\nu_p \sim E_g$, and $h\nu_p < E_g$, respectively. The solid blue arrows in the middle indicate the possible transitions of electrons upon excitations and their corresponding rate constants k_i. The purple dotted arrows represent all the possible absorption transitions, labeled with their corresponding absorption strength α_{ij}.

consists of six energy states, E_{sv}, E_v, E_s, E_d, E_{c_1}, and E_{c_2}, which correspond to a SVB (sv), a VB (v), a shallow defect state (s), a deep defect state (d), the bottom of the CB (c_1), and a higher CB energy state (c_2), respectively. Here $E_g = E_{c_1} - E_v$ and $E_l = E_{c_2} - E_v$. The optical absorptions occur between the following states (dotted arrows in Figure 4): $E_{sv} \rightarrow E_v$, $E_v \rightarrow E_{c_1}$, $E_v \rightarrow E_{c_2}$, $E_s \rightarrow E_{c_1}$, $E_s \rightarrow E_{c_2}$, $E_d \rightarrow E_{c_1}$ and $E_d \rightarrow E_{c_2}$. When the electrons in the E_v state are excited to E_{c_1} or E_{c_2} states, i.e., $h\nu_p > E_l$, several decay mechanisms exist: a rapid decay from E_{c_2} to E_{c_1} with a rate of k_0; the transition of electrons from E_{c_1} to all the lower energy states, E_v, E_s, and E_d, all with a relatively fast rate k_1; the electrons in states E_s and E_d decay back to the E_v state with rates of k_2 and k_3, respectively. Note that it is possible that the transitions from E_{c_1} to E_d, E_{c_1} to E_s, and E_{c_1} to E_v may occur at different times that are shorter than the resolved time constant ($\tau_1 \sim 0.34$ ps), but since they are within the time resolution of the experiment, they are considered to be the same.

The CB minimum is considered to be at $E_{c_1} = 2.2$ eV, which is based on the experimentally determined Tauc direct band gap of 2.2 eV (Figure 1). A higher CB state E_{c_2} at 2.7 eV is introduced because of the following facts: (1) in the direct band Tauc plot (Figure 1), there is another linear region which gives an intersection at 2.8 eV. This experimental result suggests a second intrinsic CB in CuO; (2) the TAS spectra always have a photobleaching dip at 2.7 eV, independent of $h\nu_p$.

Moreover, as shown in Figure S2, the broad dip consists of two different dips at 2.23 and 2.67 eV; (3) according to a cluster theory calculation on square CuO_4 clusters within CuO as the basic units, there exists an energy state 0.5 eV higher than E_{c_1} due to the $b_{1g}-e_u(\pi)$ transition.[41]

The two defect states, E_s and E_d, are proposed based on the following reasons: (1) the existence of the two long lifetimes in the TAS analysis, $\tau_2 \sim 170$ ns and $\tau_3 \sim 2.8$ μs; in solid-state materials, these long lifetimes usually belong to defect state transitions.[37,42−44] Therefore, the two long time constants most likely correspond to the kinetics involving a shallow and a deep defect state; (2) based on the TAS results, $\Delta A(\nu,t)$ is positive at $h\nu < E_g$, which can be realized through the absorption of intragap energy states that could be defect states; (3) based on the DFT calculations, defect-induced states due to copper vacancy, V_{cu}^{-1}, and oxygen substitutional, O_{Cu}^{-1}, lie at ~0.5 eV above the E_v,[45] which is consistent with E_U; (4) previous DFT calculations have also revealed that defects like oxygen substitutional O_{cu}^{-2}, oxygen interstitial O_i^{-1}, and copper vacancy V_{cu}^{-2} could introduce energy levels at ~1 eV above E_v.[45] These deep defect states could correspond to E_d. Therefore, in the model, we assume $E_s = 0.5$ eV and $E_d = 1$ eV relative to E_v. These two defect states could originate from bulk defects such as vacancies, point defects, as well as grain and grain boundaries. It is worth noting that the difference in grain boundary characteristics can lead to a variation in defects properties. For instance, it has been shown that an increase in grain boundary area is correlated with longer recombination lifetimes in Cu_2S thin films.[46] For NiO[47] and perovskite solar cells,[48] the grain boundaries have a detrimental impact on the charge separation by mediating the electron and hole recombination. The grain boundaries can also induce surface states in the band gap of Si/SiO_x, resulting in a red shift in the ground state bleaching as crystalline domain sizes decrease.[49]

The SVB, E_{sv}, is introduced based on the following evidence: (1) the ns-TAS spectra reveal the appearance of a positive $\Delta A(\nu,t)$ at $h\nu > 3$ eV (see Figure 2). Such an energetic peak should correspond to a transition between two intrinsic states which has also been attributed to the transition from the SVB to the VB in the literature;[18,29] (2) the steady-state optical absorption (Figure S1) increases monotonically with $h\nu$, indicating strong high energy transitions above 3 eV; (3) a

https://doi.org/10.1021/acsami.2c22595
ACS Appl. Mater. Interfaces 2023, 15, 18414−18426

Table 1. Rate Equations and Initial Conditions for the 3 Excitation Cases

	$h\nu_p > E_l$	$h\nu_p \sim Eg$, $h\nu_p < Eg$
rate equations	$\frac{\partial \Delta n_v(t)}{\partial t} = k_1 \Delta n_{c_1}(t) + k_2 \Delta n_s(t) + k_3 \Delta n_d(t)$	$\frac{\partial \Delta n_v(t)}{\partial t} = k_1 \Delta n_{c_1}(t) + k_2 \Delta n_s(t) + k_3 \Delta n_d(t)$
	$\frac{\partial \Delta n_s(t)}{\partial t} = k_1 \Delta n_{c_1}(t) - k_2 \Delta n_s(t)$	$\frac{\partial \Delta n_s(t)}{\partial t} = k_1 \Delta n_{c_1}(t) - k_2 \Delta n_s(t)$
	$\frac{\partial \Delta n_d(t)}{\partial t} = k_1 \Delta n_{c_1}(t) - k_3 \Delta n_d(t)$	$\frac{\partial \Delta n_d(t)}{\partial t} = k_1 \Delta n_{c_1}(t) - k_3 \Delta n_d(t)$
	$\frac{\partial \Delta n_{c_1}(t)}{\partial t} = k_0 \Delta n_{c_2}(t) - 3k_1 \Delta n_{c_1}(t)$	$\frac{\partial \Delta n_{c_1}(t)}{\partial t} = -3k_1 \Delta n_{c_1}(t)$
	$\frac{\partial \Delta n_{c_2}(t)}{\partial t} = -k_0 \Delta n_{c_2}(t)$	$\frac{\partial \Delta n_{c_2}(t)}{\partial t} = 0$
initial conditions	$\Delta n_v(t=0) = -\Delta n$	$\Delta n_v(t=0) = -\Delta n$
	$\Delta n_s(t=0) = 0$	$\Delta n_s(t=0) = 0$
	$\Delta n_d(t=0) = 0$	$\Delta n_d(t=0) = 0$
	$\Delta n_{c_1}(t=0) = 0$	$\Delta n_{c_1}(t=0) = \Delta n$
	$\Delta n_{c_2}(t=0) = \Delta n$	$\Delta n_{c_2}(t=0) = 0$

photoelectrochemical study shows that the VB of CuO consists of two separated VBs, a top VB made from 3d orbitals of Cu^{+2} and an SVB due to an oxygen-2p-type band located at ∼2 eV below E_v.[50] In our ns-TAS measurements, this positive peak appears at 3.2 eV, which could belong to the SVB to VB absorption; thus, in the model, the SVB is set to $E_{sv} = -3.2$ eV.

For the non-equilibrium transition of electrons, it is assumed that $k_0 > k_1 \gg k_2 > k_3$, where k_j $(j = 0, 1, 2, 3)$ is the rate constant of the corresponding transition, which is defined as $k_j = \frac{1}{\tau_j}$ (where $j = 0, 1, 2, 3$) (in Section 4.3 we will show that these rate constants correspond to the experimentally obtained time constants). In the case of photoexcitation to E_{c_2}, in relaxation to E_{c_1}, electrons undergo coherent processes, such as momentum scattering, carrier−carrier scattering, intravalley scattering, and hole-optical phonon scattering, all of which occur in ≤∼200 fs;[51−53] hence, a single ultrafast rate constant k_0 is defined to account for these effects. Note that the timescale of these processes lies within the instrument response time of the measurements; thus, k_0 is not resolvable in this study. In the literature, the trapping timescale of metal oxides, such as BiVO4,[54] SnO_2,[43] and TiO_2,[44] is reported to be few ps when electrons fall from the CB minimum to the defect/trap states, . Thus, the second fastest rate constant is associated with the decay of E_{c_1} to the low-lying energy states and is denoted as k_1 in the model. Moreover, the timescale of the recombination of the charge carrier in shallow traps is reported to be 5−12 ns for TiO_2[37] and 3.1 ns for WSe_2,[38] while the deep traps have a lifetime of 7 μs for TiO_2[39] and 1−10 μs in a metal halide perovskite;[40] moreover, in CuO, a time constant of >50 ps is associated with the recombination of electrons and holes.[18,19] Thus, in the current study, the experimentally observed $\tau_2$and τ_3 are assumed to originate from the de-trapping of electrons from the shallow and deep trap states, and the decay rates are denoted by k_2 and k_3, respectively. It is worth noting that there is no observable transition between the defect states because of their low density and spatially separated locations in thin films.

4.2. Rate Equations and Solutions. Due to different $h\nu_p$, three sets of rate equations can be established based on the proposed transition energy diagram and are summarized in Table 1 with their corresponding initial conditions. Here, $\Delta n_i(t)$ (i = v,s,d,c_1,c_2) is the nonequilibrium electron population of the energy level i at time t after excitation, k_j(j = 0, 1, 2, 3) is the rate constant of the corresponding transition, and Δn denotes the total number density of the photoexcited electrons by the excitation beam. For the experimental spectra as shown in Figure 2, since the spectra were normalized according to the absorbed photon flux at $h\nu_p$ (assuming an effective quantum efficiency of 100%, i.e., each absorbed photon generates an electron−hole pair), the same Δn is used for all the three $h\nu_p$ cases. For the case of $h\nu_p \sim E_g$ and $h\nu_p < E_g$, both the rate equations and the initial conditions are exactly the same since for $h\nu_p < E_g$, we assume that electrons from the VB tails are excited to E_{c_1}, and the VB and VB tail are treated as a single state. Such an assumption is based on the multiple experimental evidence of measured IPCE (incident photon conversion efficiency) spectra for CuO, where the incident photon with an energy lower than the band gap can still introduce a photocurrent.[55,56] However, for $h\nu_p > E_l$, both the initial conditions and the rate equations are different from the other two cases since an additional energy state, E_{c_2}, is involved in the charge dynamics.

The complete solutions of the rate equations are provided in Table S1 of the Supporting Information. As expected, the solutions for $h\nu_p \sim E_g$ and $h\nu_p < E_g$ cases are identical, while the solutions for the $h\nu_p > E_l$ case are significantly different. For $h\nu_p > E_l$, Δn_{c_2} is dominated by k_0, and all other solutions for $\Delta n_i(t)$(i = v, s, d, c_1) contain an exponential decay function of $e^{-k_0 t}$, while for the other two cases, $\Delta n_{c_2} = 0$. Since $k_0 > k_1 \gg k_2 > k_3$, at a sufficiently long time t, $e^{-k_0 t} \to 0$, and thus, it is interesting to notice that the solutions eventually become the same for both the $h\nu_p > E_l$ case and the $h\nu_p \sim E_g$ or $h\nu_p < E_g$ case; i.e., at a sufficiently long initial delay time, the solutions of all the cases are exactly the same.

Based on the lattice properties of the CuO crystal, the equilibrium population parameters are estimated in Section S6 of the Supporting Information. The total electron population, $n_i = \Delta n_i + n_{i\infty}$ (where i = v,s,d,c_1,c_2, and $n_{i\infty}$ is the equilibrium population), for different energy states can be obtained and are plotted in Figure 5, where the equilibrium populations,

https://doi.org/10.1021/acsami.2c22595
ACS Appl. Mater. Interfaces 2023, 15, 18414−18426

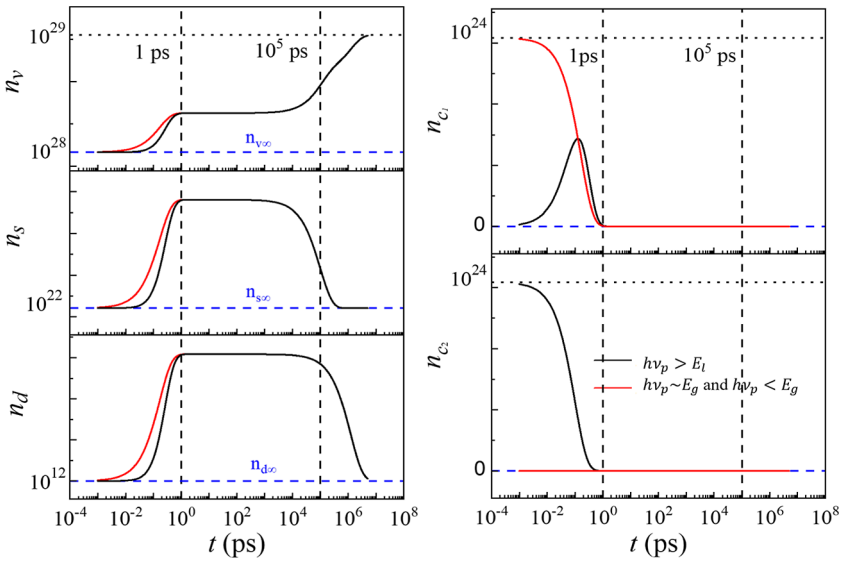

Figure 5. Total electron population at different energy states under 3 excitations. Black: $h\nu_p > E_l$, red: $h\nu_p \sim E_g$ and $h\nu_p < E_g$. The equilibrium populations, $n_{v\infty}$, $n_{s\infty}$, and $n_{d\infty}$, are denoted by the horizontal blue dashed lines. The initial population of the CBs are assumed to be zero in the model.

$n_{v\infty}$,$n_{s\infty}$, and $n_{d\infty}$, are denoted by the horizontal blue dashed lines. Note that $n_{c_{1\infty}} = n_{c_{2\infty}} = 0$ in the calculation.

The populations from the solution of the rate equations are plotted in Figure 5. The time constants $\tau_1 = 0.5$ ps, $\tau_2 = 170$ ns, and $\tau_3 = 2.8$ μs are taken as the average of the fitted values in the 3 excitation cases from Figure 3d–f and τ_0 is set to 0.1 ps. Figure 5 reveals two common features regardless of the $h\nu_p$: (1) the entire timescale can be divided into 3 stages: stage#1 ultra-fast stage (t < 1 ps), where the populations of the electrons in all the energy states change rapidly; stage #2 quasi-static stage (1 ps < t < 100 ns), where all the populations remain almost constant; stage #3 recovery stage (t > 100 ns), where the populations approach the equilibrium values. These stages are consistent with the three stages observed experimentally (Figure 3). (2) for t < 1 ps, n_v, n_s, and n_d increase rapidly to a quasi-equilibrium value, whereas n_{c_1} and n_{c_2} decrease to 0. These common behaviors reflect the intrinsic charge dynamics governed by the three time constants; upon excitations, all the electron populations are driven away from equilibrium, and the dynamics of the electrons are governed by the smallest time constant at small t. However, since there is no transition in the ps to ns timescale, n_v, n_s, and n_d would remain unchanged until a later time; when defect states release the trapped electrons to the VB, n_s, n_d, and n_d start to acquire their equilibrium values. There are two significant differences between the case of $h\nu_p > E_l$ and the cases of $h\nu_p \sim E_g$, and $h\nu_p < E_g$: (1) for t < 1 ps, the rise of n_v, n_s, and n_d is faster for the cases of $h\nu_p \sim E_g$ and $h\nu_p < E_g$ compared to that of $h\nu_p > E_l$; (2) the behaviors of n_{c_1} and n_{c_2} are very different. n_{c_1} shows a peak for the $h\nu_p > E_l$ case since in the first few hundred femtoseconds, the hot electrons in E_{c_2} relax to E_{c_1}, causing a spike in n_{c_1}, and a sharp decrease in n_{c_2}. The observed difference between the $h\nu_p > E_l$ excitation case and those of $h\nu_p \sim E_g$ and $h\nu_p < E_g$ is because there is no relaxation from E_{c_2} to E_{c_1} in the latter two cases, and hence, the decay of the electrons from E_{c_1} to E_v, E_s, and E_d occurs instantaneously after the photoexcitation; so, compared to the case of $h\nu_p > E_l$, n_v, n_s, and n_d undergo a steeper rise in the beginning. The populations for the longer timescale are identical in all three cases since the transitions in the ns to μs timescale are identical.

4.3. Modeling of Transient Absorption $\Delta A(\nu,t)$. Based on the solutions of the rate equations, the optical absorption $A_{ij}(t)$ from the ith state to the jth state with a resonance frequency $\nu_{ij} = \frac{E_j - E_i}{h}$ (E_j and E_i are the energy of the jth and ith energy levels, respectively) can be written as

$$A_{ij}(t) = \sigma_{i\to j} n_i(t)(N_j - n_j(t)) \tag{5}$$

where $\sigma_{i\to j}$ is the absorption cross section; $n_i(t)$ and $n_j(t)$ are the population of the initial and final states at time t, respectively; and N_j is the total number of available states in E_j. Ideally, the absorption spectrum can be written as

$$A(\nu, t) = \sum A_{ij}(t)\delta(\nu - \nu_{ij}) \tag{6}$$

where the summation runs over all the possible allowed absorption transitions and $\delta(-\nu_{ij})$ is the δ-function, resembling the discretized spectral lines. However, due to carrier scattering, thermal fluctuations, and other spectral line broadening mechanisms, the actual spectral line shape is not a δ-function but usually can be represented by a Lorentzian shape or other spectral shapes. Here, we use the Lorentzian spectral shape $S_{ij}(\nu)$

$$S_{ij}(\nu) = \frac{\gamma_{ij}}{2\pi\left(h^2(\nu - \nu_{ij})^2 + \left(\frac{1}{2}\gamma_{ij}\right)^2\right)} \tag{7}$$

where γ_{ij} is the oscillation damping factor which determines the absorption peak widths, varying for different transitions. Then, according to eq 1, the TAS spectrum is determined. Based on Figure 4, there are seven possible absorptions that can contribute to the final transient absorption spectra, and the overall $\Delta A(\nu,t)$ can be written theoretically as

https://doi.org/10.1021/acsami.2c22595
ACS Appl. Mater. Interfaces 2023, 15, 18414−18426

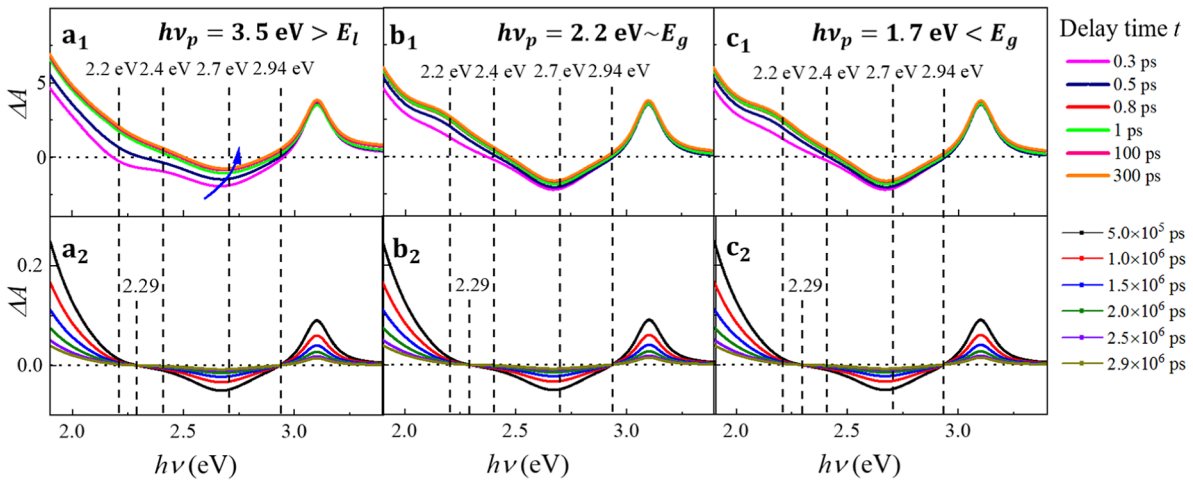

Figure 6. Modeled ps- and ns-TAS spectra $\Delta A(\nu,t)$at different delay times t under (a) $h\nu_p$ = 3.5 eV > E_l, (b) $h\nu_p$ = 2.2 eV ~ E_g, and (c) $h\nu_p$ = 1.7 eV < E_g. Top row: ps-TAS spectra; bottom row: ns-TAS spectra.

$$\begin{aligned}\Delta A(\nu, t) = {} & \Delta A_{sv\to v}(\nu, t) + \Delta A_{v\to c_1}(\nu, t) \\ & + \Delta A_{v\to c_2}(\nu, t) + \Delta A_{s\to c_1}(\nu, t) \\ & + \Delta A_{s\to c_2}(\nu, t) + \Delta A_{d\to c_1}(\nu, t) \\ & + \Delta A_{d\to c_2}(\nu, t) \end{aligned} \quad (8)$$

Note that there is no absorption between the shallow and deep defect states as they are spatially separated, and a direct transition is less probable. Considering eqs 1 and 5−8, $\Delta A(\nu,t)$ is given by

$$\begin{aligned}\Delta A(\nu, t) = {} & S_{sv}(\nu)\sigma_{sv\to v}[n_{sv}(t)(N_v - n_v(t)) - n_{sv\infty}(N_v - n_{v\infty})] \\ & + S_{vc_1}(\nu)\sigma_{v\to c_1}[n_v(t)(N_{c_1} - n_{c_1}(t)) - n_{v\infty}(N_{c_1} - n_{c_1\infty})] \\ & + S_{vc_2}(\nu)\sigma_{v\to c_2}[n_v(t)(N_{c_2} - n_{c_2}(t)) - n_{v\infty}(N_{c_2} - n_{c_2\infty})] \\ & + S_{sc_1}(\nu)\sigma_{s\to c_1}[n_s(t)(N_{c_1} - n_{c_1}(t)) - n_{s\infty}(N_{c_1} - n_{c_1\infty})] \\ & + S_{sc_2}(\nu)\sigma_{s\to c_2}[n_s(t)(N_{c_2} - n_{c_2}(t)) - n_{s\infty}(N_{c_2} - n_{c_2\infty})] \\ & + S_{dc_1}(\nu)\sigma_{d\to c_1}[n_d(t)(N_{c_1} - n_{c_1}(t)) - n_{d\infty}(N_{c_1} - n_{c_1\infty})] \\ & + S_{dc_2}(\nu)\sigma_{d\to c_2}[n_d(t)(N_{c_2} - n_{c_2}(t)) - n_{d\infty}(N_{c_2} - n_{c_2\infty})] \end{aligned} \quad (9)$$

Equation 9 includes all of the absorption transitions shown in Figure 4. However, due to the finite spectral width, each resonant absorption could only significantly contribute to the absorption in a wavelength range near its resonant frequency, i.e., $\nu_{ij} - 2\gamma_{ij} \le h\nu \le \nu_{ij} + 2\gamma_{ij}$, which means at a particular $h\nu$, not all the 7 absorption transitions in eq 9 need to be considered. As described in the next section, tihe γ_{ij} values are smaller than 0.5 eV, so only a limited number of resonant absorption peaks near $h\nu$ need to be considered. For instance, Section S7 of the Supporting Information shows the explicit expressions for $\Delta A(\nu,t)$ at $h\nu$ = 2.2 eV (eq S4) and $h\nu$ = 2.7 eV (eq S6) in the $h\nu_p \sim E_g$ excitation case; only 4 or 2 resonant transitions are considered. By further considering $k_1 \gg k_2 > k_3$, the final expression of $\Delta A(\nu,t)$ only depends on the three time-dependent exponential functions, e^{-3k_1t}, e^{-k_2t}, and e^{-k_3t}, respectively. The results show that independent of the spectral region, $\Delta A(\nu,t)$ can be expressed as the sum of 3 time-dependent exponential functions with time constants which are directly related to the experimentally resolved time constants. Thus, $k_j = 1/\tau_j$ is validated.

Clearly, based on the solutions of the rate equations, once both the values of $\sigma_{i\to j}$ and γ_{ij} for each absorption transitions are determined, one should be able to model $\Delta A(\nu,t)$. In order to obtain these two sets of parameters, a spectral analysis strategy based on the experimental ps-TAS $\Delta A(\nu,t)$ for the $h\nu_p$ = 3.5 eV > E_l case is employed, and the details are explained in Section S8 of the Supporting Information. The results are presented in Figures S5 and S6, and the corresponding video for the spectral fittings is provided as Movie M1. The plots of the fitted energy levels, E_i, and damping constants, γ_{ij}, versus decay time t (Figure S7a,b) show that these two sets of parameters are invariant with respect to t. Further analysis of the absorption cross sections, $\sigma_{i\to j}$, based on the solutions of the rate equations (Table S1) shows that all $\sigma_{i\to j}$, corresponding to the different absorption transitions in Figure 4, converge to constant values at $t \ge 1$ ps, and those values are used in the spectral modeling. All the parameters used to model the $\Delta A(\nu,t)$ for different $h\nu_p$ cases and from ps to μs timescales based on eq 9, and the solutions of the rate equations (Table S1), are listed in Table S2.

Figure 6 shows the modeled TAS spectra $\Delta A(\nu,t)$ under the 3 excitation cases based on eq 9, the solution of the rate equations, and parameters in Tables S1 and S2. For all three cases, the Δn values are assumed to be the same, 2.5 × 10^{24} m^{-3}. In the case of $h\nu_p > E_l$, as shown in Figure 6a_1, similar to the experimental results (Figure 2a_1), four main spectral features are observed in ps-TAS: (1) positive $\Delta A(\nu,t)$ at $h\nu$ < ~2.2−2.4 eV; (2) positive ΔA at $h\nu$ > ~ 2.9 eV and a peak at 3.1 eV; (3) a broad dip at ~2.67 eV with an initial width of ~0.8 eV; and (4) a slight blue shift of the dip position as indicated by the blue arrow in the figure. As t increases up to 0.5 ps, the entire spectra move up, then remain fairly steady, consistent with the experimental $\Delta A(\nu,t)$. For the ns-TAS spectra as shown in Figure 6a_2, three features are observed: (1) positive $\Delta A(\nu,t)$ at $h\nu$ > 3 eV and a peak at 3.1 eV; (2) positive $\Delta A(\nu,t)$ at $h\nu$ < 2.3 eV; and (3) a broad dip at 2.3 eV < $h\nu$ <3 eV, which is centered at ~2.7 eV. Other experimental features are also captured, including the time invariance of the dip width and position, and all the $\Delta A(\nu,t)$ values approach zero with time. The normalized $\Delta A(\nu,t)$ spectra are plotted in Figure S9a, similar to the normalized experimental spectra shown in Figure S3a; the time-dependent trends in spectral shape are the same: for ps-TAS spectra, the spectral shape

https://doi.org/10.1021/acsami.2c22595
ACS Appl. Mater. Interfaces 2023, 15, 18414−18426

changes significantly, especially in the $h\nu$ < 2.0−2.4 eV region, and all the normalized positive $\Delta A(\nu,t)$ values increase with t; for ns-TAS, the normalized spectra are invariant with time.

The ps-TAS $\Delta A(\nu,t)$ for the $h\nu_p \sim E_g$ case, as shown in Figure 6b$_1$, has quite similar features to the experimental results (Figure 2b$_1$), with positive $\Delta A(\nu,t)$ values at $h\nu$ < ~2.0−2.4 eV, and a broad negative dip centered at ~2.67 eV. The only difference is the distinguished peak at 3.1 eV. The time dependence of ns-TAS spectra is similar to those shown in Figures 2b$_2$ and 6a$_2$. The normalized ps-TAS and ns-TAS spectra shown in Figure S9b are also consistent with those observed experimentally (Figure S3b) and for the $h\nu_p > E_l$ case. For the $h\nu_p < E_g$ case as shown in Figure 6c$_1$,c$_2$, since the solutions for the rate equations are exactly the same for the $h\nu_p \sim E_g$ case, the time-dependent TAS spectral behaviors are identical to those shown in Figure 6b$_1$,b$_2$.

The time traces of the modeled spectra for different excitation cases at selected $h\nu$ values ranging from 2.1 to 3.0 eV are plotted in Figure 7. For all $h\nu_p$ cases, the trends of

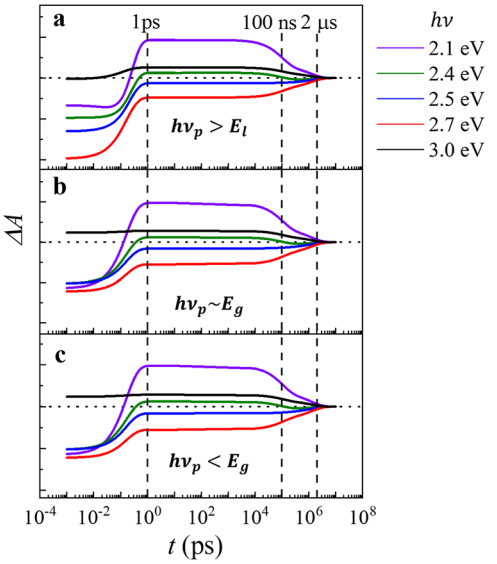

Figure 7. Time traces of the model spectra at different probe energies ($h\nu$) under (a) $h\nu_p > E_l$, (b) $h\nu_p \sim E_g$, and (c) $h\nu_p < E_g$. The dashed lines indicate the approximate time to divide the whole timescale into three stages.

different time traces are similar at different $h\nu$: there is an initial rise in $\Delta A(\nu,t)$ within the first 1 ps, then the time traces plateau within 1 ps ≤ t ≤ ~10 ns, and finally $\Delta A(\nu,t)$ approaches zero at t ≥ ~10 ns. Similar to the experimental time traces, at the low energy region, $h\nu$ < 2.4 eV, which is represented by $h\nu$ = 2.1 eV, $\Delta A(\nu,t)$ undergoes a rise and moves away from equilibrium but returns back to zero in the μs timescale. The time trace near the low energy isosbestic point, $h\nu \sim$ 2.4 eV, follows the same trend. $\Delta A(\nu,t)$ values in the broad dip region, represented by $h\nu$ = 2.5 and 2.7 eV, remain negative throughout the entire time range, as expected, and approach zero (equilibrium) in the μs timescale. In the high energy region, as represented by $h\nu$ = 3.0 eV, $\Delta A(\nu,t)$ slightly increases at t ≤ 1 ps for the $h\nu_p > E_l$ case, plateaus, and recovers to zero in the μs timescale. For the $h\nu_p \sim E_g$ and $h\nu_p < E_g$ cases, the $\Delta A(\nu,t)$ value at $h\nu$ = 3.0 eV remains almost a constant for t ≤ 10 ns and then approaches zero at t > 100 ns. The reason for this difference is that in the case of $h\nu_p > E_l$, the electrons are initially excited to E_{c_2} and decay to E_{c_1} within 0.1 ps; thus, the transitions to the low-lying energy levels are delayed compared to the other two cases.

The modeled spectra $\Delta A(\nu,t)$ not only successfully capture the main features of the experimental TAS spectra but can also be directly compared to the experimental spectra after rescaling by Δn. Movies M2, M3, and M4 show the direct comparison of the modeled spectra (blue curves) and the experimental spectra (black curves), from the sub-ps to μs timescale for three $h\nu_p$ cases. All the contributions due to absorptions from different intrinsic transitions marked in Figure 4 are shown as dashed red curves for ps-TAS. Regardless of the $h\nu_p$, two general trends are observed: when t < 1 ps, there are relative large discrepancies between the modeled spectra and the experimental spectra, especially in $h\nu$ < 2.4 eV; when t > 1 ps, the modeled spectra and the experimental spectra match very well. These results show that our model (Figure 4) and the solution of the rate equations are reasonable to explain both the spectral shape and the time dependence of the experimental TAS for relatively long time delays (t > 1 ps). But there may be some other mechanisms that are missing in the short time period. Physically at t < 1 ps, many electrons from VB are excited to CB, and there is a significant amount of photo-generated free electrons in the material. Thus, one possible contribution for the discrepancies observed in Movies M2, M3, and M4 is the free-electron absorption (FEA), which can be described by[57]

$$\Delta A_f = A_1\nu^{-1.5} + A_2\nu^{-2.5} + A_3\nu^{-3.5} \quad (10)$$

where ΔA_f is the TAS due to the FEA and A_i (i = 1, 2, 3) are the related constants. The first power-law term in eq 10 is due to the electron scattering by acoustic phonons, the second power-law term comes from electron scattering by optical phonons, and the last term is due to the scattering by ionized impurities.[57] The effect of the FEA in the ps-TAS spectra can be estimated by fitting the difference between the modeled spectra and corresponding experimental spectra at $h\nu$ < 2.4 eV for t ≤ 1 ps by eq 10, and the results are presented in Movies M5, M6, and M7. Based on the fits, the A_i coefficients in eq 10 are estimated as, $A_1 = A_2 = 0$, regardless of the excitation energy, and $A_3 = 7.6 \times 10^{-10}$, 3.4×10^{-10}, and 0.7×10^{-10} for $h\nu_p$ = 3.5, 2.2, and 1.7 eV, respectively. The estimated ΔA_f is then added back to the corresponding modeled spectra at t < 1 ps. Movies M8, M9, and M10 show the comparison of the FEA-corrected spectra and experimental TAS spectra. Clearly, the agreement between the modeled spectra and experimental spectra is improved.

5. CONCLUSIONS

In this work, we have presented a thorough understanding of the charge dynamics of a CuO thin film by reproducing the experimental TAS $\Delta A(\nu,t)$ with a model based on rate equations which successfully capture the main observed experimental features. This study implies that, in order to gain a complete insight into the charge dynamics, (1) TAS measurements should be performed in a broad timescale and excitation energy range, and (2) the TAS analysis should be accompanied by appropriate models, i.e., rate equations based on reasonable assumptions.

The TAS experiments were done in a broad timescale, from ps to μs, and under three different excitation energies: above, near, and below the band gap. Regardless of the excitation

https://doi.org/10.1021/acsami.2c22595
ACS Appl. Mater. Interfaces 2023, 15, 18414−18426

energy, the main spectral features remained consistent with time. $\Delta A(\nu,t)$ was positive at low and high energies, while there was a very broad negative dip, centered at ∼2.7 eV which was proven to consist of two overlapping dips at 2.2 and 2.7 eV by performing the TAS measurements at a different spot of the sample and a careful analysis of the UV−vis spectrum. To have a closer look at the spectral changes with time, the ps- and ns-TAS spectra were normalized by the value of the absolute minimum. The results showed that in the normalized ps-TAS $\Delta A(\nu,t)$, the spectra slightly changed with time at low energies, while the normalized ns-TAS $\Delta A(\nu,t)$ was time independent, indicating that the mechanism of the charge dynamics remains the same in the ns to μs timescale. To gain a better understanding of the charge dynamics, the time traces were analyzed at different probe energies. Independent of the excitation energy, three regions were identified: (1) ultra-fast region ($t < 1$ ps); (2) quasi-static region ($1 \leq t \leq 100$ ns); and (3) recovery region ($t < 100$ ns), where in the ultra-fast region, time traces quickly increased, then plateaued in the quasi-static region, and approached zero (equilibrium) in the recovery region. Regardless of the excitations, three time constants, $\tau_1 \sim$ 0.34−0.59 ps, $\tau_2 \sim$ 162−175 ns, and $\tau_3 \sim$ 2.5−3.3 μs, were resolved, indicating the dominating charge dynamics in very different timescales.

Based on the TAS $\Delta A(\nu,t)$, UV−vis, and previous studies, a compelling transition energy diagram was proposed which consists of a higher energy CB, E_{c_2}; shallow and deep defect states, E_s and E_d, respectively; and an SVB state. The higher CB, E_{c_2}, was proposed based on the observation of a double dip in the ps-TAS $\Delta A(\nu,t)$ as well as the analysis of the Tauc plot. The defect states were introduced because of the existence of grain boundaries in the crystal that break the periodicity of the lattice and induce defect states. The existence of such defect states has also been supported in previous DFT studies. The SVB was considered due to the observation of an energetic peak in the ps- and ns-TAS $\Delta A(\nu,t)$ as well as the energetic high intensity absorption in the UV−vis spectra. A decay mechanism was proposed such that upon excitation by the ultra-fast pulse above E_{c_2}, the electrons decay very quickly ($t < 100$ fs) to E_{c_1} and then decay to the defect states and the VB within 0.5 ps. The de-trapping from the shallow and deep defect states to the VB was considered to occur in ∼170 ns and 2.8 μs, respectively, which were found from the averages of the long time constants in the 3 different excitation energies.

The experimental TAS $\Delta A(\nu,t)$ were modeled by solving the rate equations based on the proposed energy diagram and the corresponding transitions, and a simple expression for the $\Delta A(\nu,t)$ was defined by assuming a Lorentzian function for the spectral shape of the transitions. The parameters of the model were found by fitting the spectra of the $h\nu_p = 3.5$ eV excitation case to the derived $\Delta A(\nu,t)$. The modeled time-dependent spectra were explicitly compared to the experimental TAS $\Delta A(\nu,t)$ as shown by the videos which indicated a very good agreement at $t > 1$ ps. As a plausible mechanism to explain the inconsistencies at $t < 1$ ps, free-electron absorption was investigated and applied to the model which improved the agreement and thus can be considered a contributing mechanism in the very short timescale.

The proposed approach in this study, i.e., using a broad timescale and different excitation energies in the TAS measurements, and the complementary model based on the rate equations successfully elucidated the charge dynamics of the CuO thin film. However, one should note that the model is only valid within the introduced assumptions. For instance, the band tails are considered as single energy states instead of continuous bands, and all the decay mechanisms, i.e., recombination, are assumed to be of the first order. Considering these assumptions, the model can be generalized to other materials given that it is necessary to have a priori knowledge about the optical properties, i.e., band gap, of the system as well as the intra-gap energy states, i.e., defect states.

A future study could be thickness-dependent measurements to evaluate the effect of film thickness on the dynamics of photo-induced charge dynamics. This is because, in addition to electron−hole recombination, carrier diffusion within the film is also affected by the film's thickness. Moreover, the variation of pump light intensity across the film's depth can create a depth-dependent concentration gradient of photo-induced electrons, which would be more prominent in thicker films.

■ ASSOCIATED CONTENT

Supporting Information

The Supporting Information is available free of charge at https://pubs.acs.org/doi/10.1021/acsami.2c22595.

- Experimental spectral fittings of ps-TAS spectra for the 3.5 eV case to extract the simulation parameters (MP4)
- Comparison of the simulated TAS spectra versus the experimental spectra in the ps to μs timescale for the $h\nu_p = 3.5$ eV case (MP4)
- Comparison of the simulated TAS spectra versus the experimental spectra in the ps to μs timescale for the $h\nu_p = 2.2$ eV case (MP4)
- Comparison of the simulated TAS spectra versus the experimental spectra in the ps to μs timescale for the $h\nu_p = 1.7$ eV case. (MP4)
- Free electron absorption analysis for the $h\nu_p = 3.5$ eV case (MP4)
- Free electron absorption analysis for the $h\nu_p = 2.2$ eV case (MP4)
- Free electron absorption analysis for the $h\nu_p = 1.7$ eV case (MP4)
- Comparison of the FEA-corrected simulated TAS spectra versus the experimental spectra in the ps to μs timescale for the $h\nu_p = 3.5$ eV case (MP4)
- Comparison of the FEA-corrected simulated TAS spectra versus the experimental spectra in the ps to μs timescale for the $h\nu_p = 2.2$ eV case (MP4)
- Comparison of the FEA-corrected simulated TAS spectra versus the experimental spectra in the ps to μs timescale for the $h\nu_p = 1.7$ eV case (MP4)
- Steady-state absorption spectrum, double dip revealed in ps-TAS measurements, ps-TAS spectra at high energy, normalized TAS spectra, examples of time trace analysis, solution of rate equations, estimation of the initial electron populations, expression of $\Delta A(\nu,t)$, estimation of $\sigma_{i\rightarrow j}$ and γ_{ij}, normalized model spectra, and description of the videos (PDF)

■ AUTHOR INFORMATION

Corresponding Authors

Susanne Ullrich − *Department of Physics and Astronomy, University of Georgia, Athens, Georgia 30602, United States;* orcid.org/0000-0002-1828-2777; Email: ullrich@uga.edu

https://doi.org/10.1021/acsami.2c22595
ACS Appl. Mater. Interfaces 2023, 15, 18414−18426

Henning Meyer − *Department of Physics and Astronomy, University of Georgia, Athens, Georgia 30602, United States*; Email: hmeyer@uga.edu

Yiping Zhao − *Department of Physics and Astronomy, University of Georgia, Athens, Georgia 30602, United States*; orcid.org/0000-0002-3710-4159; Email: zhaoy@uga.edu

Authors

Mona Asadinamin − *Department of Physics and Astronomy, University of Georgia, Athens, Georgia 30602, United States*; orcid.org/0000-0002-4651-044X

Aleksandar Zivkovic − *Department of Earth Sciences, Utrecht University, 3548 CB Utrecht, The Netherlands*; orcid.org/0000-0003-1347-6203

Complete contact information is available at: https://pubs.acs.org/10.1021/acsami.2c22595

Author Contributions

M.A. performed all the experiments, modeling, calculations, and manuscript writing. S.U. and H.M. helped with ps- and ns-TAS measurements, spectral analysis, and manuscript writing. A.Z. provided insights into energy states of CuO. Y.Z. initiated this project, helped in spectral analysis, model discussions, and manuscript writing.

Notes

The authors declare no competing financial interest.

■ ACKNOWLEDGMENTS

This work was supported by the Laboratory Directed Research and Development (LDRD) program within the Savannah River National Laboratory (SRNL) and NSF grant CHE-1800050. M.A. And Y.Z. were partially supported by the National Science Foundation under grant no. ECCS-1808271.

■ REFERENCES

(1) Hoffmann, M. R.; Martin, S. T.; Choi, W.; Bahnemann, D. W. Environmental Applications of Semiconductor Photocatalysis. *Chem. Rev.* **1995**, *95*, 69−96.

(2) Tong, H.; Ouyang, S.; Bi, Y.; Umezawa, N.; Oshikiri, M.; Ye, J. Nano-Photocatalytic Materials: Possibilities and Challenges. *Adv. Mater.* **2012**, *24*, 229−251.

(3) Yang, X.; Wang, D. Photocatalysis: From Fundamental Principles to Materials and Applications. *ACS Appl. Energy Mater.* **2018**, *1*, 6657−6693.

(4) Gurylev, V. Photocatalysis: Fundamentals. In *Nanostructured Photocatalyst Via Defect Engineering: Basic Knowledge and Recent Advances*; Gurylev, V., Ed.; Springer International Publishing: Cham, 2021, pp 1−36.

(5) Li, F.; Cheng, L.; Fan, J.; Xiang, Q. Steering the Behavior of Photogenerated Carriers in Semiconductor Photocatalysts: A New Insight and Perspective. *J. Mater. Chem. A* **2021**, *9*, 23765−23782.

(6) Hisatomi, T.; Takanabe, K.; Domen, K. Photocatalytic Water-Splitting Reaction from Catalytic and Kinetic Perspectives. *Catal. Lett.* **2015**, *145*, 95−108.

(7) Zhang, L.; Mohamed, H. H.; Dillert, R.; Bahnemann, D. Kinetics and Mechanisms of Charge Transfer Processes in Photocatalytic Systems: A Review. *J. Photochem. Photobiol., C* **2012**, *13*, 263−276.

(8) Ma, J.; Miao, T. J.; Tang, J. Charge Carrier Dynamics and Reaction Intermediates in Heterogeneous Photocatalysis by Time-Resolved Spectroscopies. *Chem. Soc. Rev.* **2022**, *51*, 5777−5794.

(9) Schneider, J.; Curti, M. Spectroscopic and Kinetic Characterization of Photogenerated Charge Carriers in Photocatalysts. *Photochem. Photobiol. Sci.* **2022**, *22*, 195−217.

(10) Xu, J.-Y.; Tong, X.; Yu, P.; Wenya, G. E.; McGrath, T.; Fong, M. J.; Wu, J.; Wang, Z. M. Ultrafast Dynamics of Charge Transfer and Photochemical Reactions in Solar Energy Conversion. *Adv. Sci.* **2018**, *5*, 1800221.

(11) Cooper, J. K.; Reyes-Lillo, S. E.; Hess, L. H.; Jiang, C.-M.; Neaton, J. B.; Sharp, I. D. Physical Origins of the Transient Absorption Spectra and Dynamics in Thin-Film Semiconductors: The Case of Bivo4. *J. Phys. Chem. C* **2018**, *122*, 20642−20652.

(12) Yoshihara, T.; Katoh, R.; Furube, A.; Tamaki, Y.; Murai, M.; Hara, K.; Murata, S.; Arakawa, H.; Tachiya, M. Identification of Reactive Species in Photoexcited Nanocrystalline Tio2 Films by Wide-Wavelength-Range (400−2500 Nm) Transient Absorption Spectroscopy. *J. Phys. Chem. B* **2004**, *108*, 3817−3823.

(13) Kollenz, P.; Herten, D.-P.; Buckup, T. Unravelling the Kinetic Model of Photochemical Reactions Via Deep Learning. *J. Phys. Chem. B* **2020**, *124*, 6358−6368.

(14) Gupta, N.; Singh, R.; Wu, F.; Narayan, J.; McMillen, C.; Alapatt, G. F.; Poole, K. F.; Hwu, S.-J.; Sulejmanovic, D.; Young, M.; et al. Deposition and Characterization of Nanostructured Cu2o Thin-Film for Potential Photovoltaic Applications. *J. Mater. Res.* **2013**, *28*, 1740−1746.

(15) Chauhan, M.; Sharma, B.; Kumar, R.; Chaudhary, G. R.; Hassan, A. A.; Kumar, S. Green Synthesis of Cuo Nanomaterials and Their Proficient Use for Organic Waste Removal and Antimicrobial Application. *Environ. Res.* **2019**, *168*, 85−95.

(16) Prabu, R. D.; Valanarasu, S.; Ganesh, V.; Shkir, M.; AlFaify, S.; Kathalingam, A.; Srikumar, S. R.; Chandramohan, R. An Effect of Temperature on Structural, Optical, Photoluminescence and Electrical Properties of Copper Oxide Thin Films Deposited by Nebulizer Spray Pyrolysis Technique. *Mater. Sci. Semicond. Process.* **2018**, *74*, 129−135.

(17) Dolai, S.; Dey, R.; Das, S.; Hussain, S.; Bhar, R.; Pal, A. K. Cupric Oxide (Cuo) Thin Films Prepared by Reactive D.C. Magnetron Sputtering Technique for Photovoltaic Application. *J. Alloys Compd.* **2017**, *724*, 456−464.

(18) Born, B.; Krupa, J. D. A.; Geoffroy-Gagnon, S.; Hristovski, I. R.; Collier, C. M.; Holzman, J. F. Ultrafast Charge-Carrier Dynamics of Copper Oxide Nanocrystals. *ACS Photonics* **2016**, *3*, 2475−2481.

(19) Shenje, L.; Larson, S.; Zhao, Y.; Ullrich, S. Composition Effects on Ultrafast Optical Properties of Cu_xO_yThin Films: A Transient Absorption Study. *J. Phys. Chem. C* **2020**, *124*, 24908−24918.

(20) Murali, D. S.; Kumar, S.; Choudhary, R. J.; Wadikar, A. D.; Jain, M. K.; Subrahmanyam, A. Synthesis of Cu2o from Cuo Thin Films: Optical and Electrical Properties. *AIP Adv.* **2015**, *5*, 047143.

(21) Pierson, J. F.; Thobor-Keck, A.; Billard, A. Cuprite, Paramelaconite and Tenorite Films Deposited by Reactive Magnetron Sputtering. *Appl. Surf. Sci.* **2003**, *210*, 359−367.

(22) Ma, P.; Yu, Y.; Xie, J.; Fu, Z. Ag3po4/Cuo Composites Utilizing the Synergistic Effect of Photocatalysis and Fenton-Like Catalysis to Dispose Organic Pollutants. *Adv. Powder Technol.* **2017**, *28*, 2797−2804.

(23) Scuderi, V.; Amiard, G.; Boninelli, S.; Scalese, S.; Miritello, M.; Sberna, P.; Impellizzeri, G.; Privitera, V. Photocatalytic Activity of Cuo and Cu2o Nanowires. *Mater. Sci. Semicond. Process.* **2016**, *42*, 89−93.

(24) Rajeshwar, K.; de Tacconi, N. R.; Ghadimkhani, G.; Chanmanee, W.; Janáky, C. Tailoring Copper Oxide Semiconductor Nanorod Arrays for Photoelectrochemical Reduction of Carbon Dioxide to Methanol. *ChemPhysChem* **2013**, *14*, 2251−2259.

(25) Schreier, M.; Héroguel, F.; Steier, L.; Ahmad, S.; Luterbacher, J. S.; Mayer, M. T.; Luo, J.; Grätzel, M. Solar Conversion of Co 2 to Co Using Earth-Abundant Electrocatalysts Prepared by Atomic Layer Modification of Cuo. *Nat. Energy* **2017**, *2*, 17087−17089.

(26) Prabhakar, R. R.; Cui, W.; Tilley, S. D. New Earth-Abundant Materials for Large-Scale Solar Fuels Generation. *Chimia* **2018**, *72*, 333.

(27) Hirst, J.; Müller, S.; Peeters, D.; Sadlo, A.; Mai, L.; Reyes, O. M.; Friedrich, D.; Mitoraj, D.; Devi, A.; Beranek, R.; Eichberger, R. Comparative Study of Photocarrier Dynamics in Cvd-Deposited

Cuwo4, Cuo, and Wo3 Thin Films for Photoelectrocatalysis. *Z. Phys. Chem.* **2020**, *234*, 699−717.
(28) Wadia, C.; Alivisatos, A. P.; Kammen, D. M. Materials Availability Expands the Opportunity for Large-Scale Photovoltaics Deployment. *Environ. Sci. Technol.* **2009**, *43*, 2072−2077.
(29) Othonos, A.; Zervos, M. Ultrafast Hole Carrier Relaxation Dynamics in P-Type Cuo Nanowires. *Nanoscale Res. Lett.* **2011**, *6*, 622.
(30) Shenje, L. T. *Femtosecond Time Resolved Excited State Spectroscopy of Photocatalytic and Biologically Relevant Systems*; University of Georgia, 2021, pp 24−46.
(31) Patterson, A. L. The Scherrer Formula for X-Ray Particle Size Determination. *Phys. Rev.* **1939**, *56*, 978−982.
(32) Langford, J. I.; Wilson, A. J. C. Scherrer after Sixty Years: A Survey and Some New Results in the Determination of Crystallite Size. *J. Appl. Crystallogr.* **1978**, *11*, 102−113.
(33) Tounsi, N.; Barhoumi, A.; Chaffar Akkari, F.; Kanzari, M.; Guermazi, H.; Guermazi, S. Structural and Optical Characterization of Copper Oxide Composite Thin Films Elaborated by Glad Technique. *Vacuum* **2015**, *121*, 9−17.
(34) Urbach, F. The Long-Wavelength Edge of Photographic Sensitivity and of the Electronic Absorption of Solids. *Phys. Rev.* **1953**, *92*, 1324.
(35) Ayik, C.; Studenyak, I.; Kranjec, M.; Kurik, M. Urbach Rule in Solid State Physics. *Int. J. Opt. Appl.* **2014**, *4*, 76−83.
(36) Acharya, S.; Chouthe, S.; Graener, H.; Böntgen, T.; Sturm, C.; Schmidt-Grund, R.; Grundmann, M.; Seifert, G. Ultrafast Dynamics of the Dielectric Functions of Zno and Batio3 Thin Films after Intense Femtosecond Laser Excitation. *J. Appl. Phys.* **2014**, *115*, 053508.
(37) Horikoshi, S.; Tsutsumi, H.; Matsuzaki, H.; Furube, A.; Emeline, A. V.; Serpone, N. In Situ Picosecond Transient Diffuse Reflectance Spectroscopy of Opaque Tio2 Systems under Microwave Irradiation and Influence of Oxygen Vacancies on the Uv-Driven/Microwave-Assisted Tio2 Photocatalysis. *J. Mater. Chem. C* **2015**, *3*, 5958−5969.
(38) Li, L.; Carter, E. A. Defect-Mediated Charge-Carrier Trapping and Nonradiative Recombination in Wse2 Monolayers. *J. Am. Chem. Soc.* **2019**, *141*, 10451−10461.
(39) Singh, M. K.; Mehata, M. S. Temperature-Dependent Photoluminescence and Decay Times of Different Phases of Grown Tio2 Nanoparticles: Carrier Dynamics and Trap States. *Ceram. Int.* **2021**, *47*, 32534−32544.
(40) Leijtens, T.; Eperon, G. E.; Barker, A. J.; Grancini, G.; Zhang, W.; Ball, J. M.; Kandada, A. R. S.; Snaith, H. J.; Petrozza, A. Carrier Trapping and Recombination: The Role of Defect Physics in Enhancing the Open Circuit Voltage of Metal Halide Perovskite Solar Cells. *Energy Environ. Sci.* **2016**, *9*, 3472−3481.
(41) Sukhorukov, Y. P.; Loshkareva, N. N.; Samokhvalov, A. A.; Moskvin, A. S. Absorption Spectra of Cuo Single Crystals near the Absorption Edge and the Nature of the Optical Gap in Copper Oxides. *J. Exp. Theor. Phys.* **1995**, *81*, 998−1002.
(42) Li, M.; Xing, G.; Xing, G.; Wu, B.; Wu, T.; Zhang, X.; Sum, T. C. Origin of Green Emission and Charge Trapping Dynamics in Zno Nanowires. *Phys. Rev. B* **2013**, *87*, 115309.
(43) Othonos, A.; Zervos, M.; Tsokkou, D. Tin Oxide Nanowires: The Influence of Trap States on Ultrafast Carrier Relaxation. *Nanoscale Res. Lett.* **2009**, *4*, 828.
(44) Serpone, N.; Lawless, D.; Khairutdinov, R. Size Effects on the Photophysical Properties of Colloidal Anatase Tio2 Particles: Size Quantization Versus Direct Transitions in This Indirect Semiconductor? *J. Phys. Chem.* **1995**, *99*, 16646−16654.
(45) Živković, A.; de Leeuw, N. H. Exploring the formation of intrinsic p-type and n-type defects in CuO. *Phys. Rev. Mater.* **2020**, *4*, 074606.
(46) Riha, S. C.; Schaller, R. D.; Gosztola, D. J.; Wiederrecht, G. P.; Martinson, A. B. F. Photoexcited Carrier Dynamics of Cu2s Thin Films. *J. Phys. Chem. Lett.* **2014**, *5*, 4055−4061.
(47) Bandaranayake, S.; Hruska, E.; Londo, S.; Biswas, S.; Baker, L. R. Small Polarons and Surface Defects in Metal Oxide Photocatalysts Studied Using Xuv Reflection−Absorption Spectroscopy. *J. Phys. Chem. C* **2020**, *124*, 22853−22870.
(48) Jacobsson, T. J.; Correa-Baena, J.-P.; Halvani Anaraki, E.; Philippe, B.; Stranks, S. D.; Bouduban, M. E. F.; Tress, W.; Schenk, K.; Teuscher, J.; Moser, J.-E.; Rensmo, H.; Hagfeldt, A. Unreacted Pbi2 as a Double-Edged Sword for Enhancing the Performance of Perovskite Solar Cells. *J. Am. Chem. Soc.* **2016**, *138*, 10331−10343.
(49) Porter, I. J.; Lee, A.; Cushing, S. K.; Chang, H.-T.; Ondry, J. C.; Alivisatos, A. P.; Leone, S. R. Characterization of Carrier Cooling Bottleneck in Silicon Nanoparticles by Extreme Ultraviolet (Xuv) Transient Absorption Spectroscopy. *J. Phys. Chem. C* **2021**, *125*, 9319−9329.
(50) Koffyberg, F. P.; Benko, F. A. A Photoelectrochemical Determination of the Position of the Conduction and Valence Band Edges of P-Type Cuo. *J. Appl. Phys.* **1982**, *53*, 1173−1177.
(51) Shah, J. Coherent Spectroscopy of Semiconductors. In *Ultrafast Spectroscopy of Semiconductors and Semiconductor Nanostructures*; Shah, J., Ed.; Springer Berlin Heidelberg: Berlin, Heidelberg, 1996, pp 27−131.
(52) Zhou, X. Q.; Cho, G. C.; Lemmer, U.; Kütt, W.; Wolter, K.; Kurz, H. Hot Carrier Relaxation in Inp and Gaas on a Subpicosecond Time Scale. *Solid-State Electron.* **1989**, *32*, 1591−1595.
(53) Sjakste, J.; Tanimura, K.; Barbarino, G.; Perfetti, L.; Vast, N. Hot Electron Relaxation Dynamics in Semiconductors: Assessing the Strength of the Electron−Phonon Coupling from the Theoretical and Experimental Viewpoints. *J. Phys.: Condens. Matter* **2018**, *30*, 353001.
(54) Pattengale, B.; Huang, J. Implicating the Contributions of Surface and Bulk States on Carrier Trapping and Photocurrent Performance of Bivo4 Photoanodes. *Phys. Chem. Chem. Phys.* **2017**, *19*, 6831−6837.
(55) Dasineh Khiavi, N.; Katal, R.; Kholghi Eshkalak, S.; Masudy-Panah, S.; Ramakrishna, S.; Jiangyong, H. Visible Light Driven Heterojunction Photocatalyst of Cuo-Cu(2)O Thin Films for Photocatalytic Degradation of Organic Pollutants. *Nanomaterials* **2019**, *9*, 1011.
(56) Tomita, R.; Pu, Z.; Kamegawa, T.; Anpo, M.; Higashimoto, S. Photoelectrochemical Properties of Copper Oxide (Cuo) Influenced by Work Functions of Conductive Electrodes. *Res. Chem. Intermed.* **2019**, *45*, 5947−5958.
(57) Pankove, J. I.; Kiewit, D. A. Optical Processes in Semiconductors. *J. Electrochem. Soc.* **1972**, *119*, 156C.

https://doi.org/10.1021/acsami.2c22595
ACS Appl. Mater. Interfaces 2023, 15, 18414−18426